

See discussions, stats, and author profiles for this publication at: <https://www.researchgate.net/publication/277706599>

Directing Anisotropic Assembly of Metallic Nanoclusters by Exploiting Linear Trio Interactions and Quantum Size Effects: Au Chains on Ag(100) Thin Films

ARTICLE *in* JOURNAL OF PHYSICAL CHEMISTRY LETTERS · MAY 2015

Impact Factor: 7.46 · DOI: 10.1021/acs.jpclett.5b00636

READS

38

2 AUTHORS:



Yong Han

Iowa State University

62 PUBLICATIONS 465 CITATIONS

SEE PROFILE



James Evans

Iowa State University

260 PUBLICATIONS 6,450 CITATIONS

SEE PROFILE

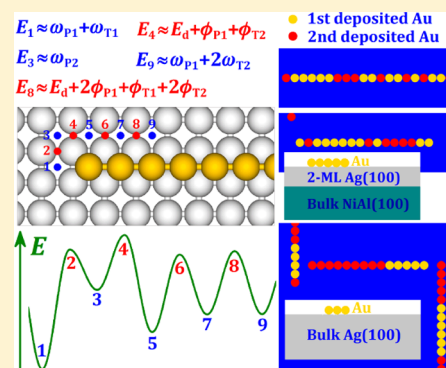
Directing Anisotropic Assembly of Metallic Nanoclusters by Exploiting Linear Trio Interactions and Quantum Size Effects: Au Chains on Ag(100) Thin Films

Yong Han* and James W. Evans

Department of Physics and Astronomy, and Division of Chemical and Biological Sciences, Ames Laboratory—U.S. Department of Energy, Iowa State University, Ames, Iowa 50011, United States

S Supporting Information

ABSTRACT: Discovery and understanding of mechanisms for kinetically controlled growth of metal nanoclusters can be enabled by realistic atomistic-level modeling with ab initio kinetics. KMC simulation of such a model for Au deposition on Ag(100) films reveals the formation of single-atom-wide Au chains below 275 K, even though 2D islands are thermodynamically preferred. Chain formation is shown to reflect a combination of strong linear trio attractions guiding assembly and a weak driving force and slow rate of transformation of 1D chains to 2D islands (or sometimes irreversible rounding of adatoms from chain sides to ends). Behavior can also be tuned by quantum size effects: chain formation predominates on 2-monolayer Ag(100) films supported on NiAl(100) at 250 K for low coverages but not on 1- or 3-monolayer films, and longer chains form than on bulk Ag(100). Our predictive kinetic modeling shows the potential for simulation-guided discovery and analysis of novel self-assembly processes.



Dramatic advances have been achieved in the experimental control of nonequilibrium shapes during the synthesis of metallic nanocrystals or nanoclusters (NCs). These shapes strongly impact, for example, catalytic or plasmonic properties. NC self-assembly via solution-phase synthesis or via deposition onto smooth surfaces can produce: 3D NCs with spherical, polyhedral, or other shapes (which are truncated for supported NCs); 2D platelets in solution or monolayer islands on surfaces; and 1D NC rods, wires, or chains.^{1–6} For solution-phase synthesis, a substantial heuristic understanding has been developed for these kinetically controlled shapes accounting for, for example, the effect of capping agents on facet energies and growth kinetics^{1,2} and the role of inhibited periphery diffusion;³ however, such synthesis is still regarded as art versus science, and detailed molecular-level understanding is lacking.¹ For assembly of epitaxial NCs on crystalline surfaces, a more detailed understanding has been achieved via atomistic lattice-gas modeling and kinetic Monte Carlo (KMC) simulation. Here there is an appreciation that the finer details of periphery diffusion, such as inhibited kink rounding, step edge crossing, or interfacet transport, strongly impact shape.^{5,6} Initial misperceptions regarding factors inducing nonequilibrium dendritic shapes,^{5,6} elongated shapes,^{7,8} and the subtle effect on shape of additives decorating the NC periphery^{5,9,10} were corrected as a result of such modeling.

Our focus in this study is on anisotropic NC shapes familiar for Au, Ag, and other metals.^{1,6} Specifically, we consider diffusion-mediated self-assembly of epitaxial Au NCs by deposition onto metal surfaces. Nanowires are often formed by deposition onto anisotropic metal^{7,8} or semiconductor^{11,12}

surfaces or onto vicinal surfaces where steps direct assembly;^{13,14} however, we will demonstrate an alternative strategy that exploits many-body adatom interactions, anticipating that linear trio attractions could induce the formation of atomic chains even on isotropic surfaces. Although many-body interactions are generally weak,^{15,16} we show that they are significant for Au and can be tuned (together with other key energetics) by exploiting quantum size effects (QSEs) to facilitate anisotropic assembly. QSE in supported metal films of a few monolayers (MLs) is associated with electron confinement, the variation of energetics reflecting commensurability of the Fermi wavelength with nanoscale film thickness.^{17,18} Prominent examples of the influence of QSEs include the formation of ultraflat deposited Ag films^{19–21} and tunable nucleation,²² reaction,²³ and oxidation^{24,25} kinetics on thin metal films.

An obstacle to experimental identification of optimal surface systems for anisotropic assembly guided by many-body interactions and QSE is the many possible combinations of deposited atoms, metallic thin films, and supports. Thus, a capability for predictive atomistic-level modeling would greatly facilitate simulation-guided discovery of appropriate systems. However, a challenge for such modeling is the need to precisely describe both system thermodynamics and also distinct barriers for terrace diffusion and for edge diffusion and corner rounding for all relevant edge configurations (barriers to which NC

Received: March 26, 2015

Accepted: May 25, 2015

Published: May 26, 2015

formation is exquisitely sensitive).^{26,27} We implement a procedure described below to obtain such barriers at the level of ab initio density functional theory (DFT). These provide precise input for KMC simulation of the NC assembly processes on the physical time scale. The Supporting Information (SI) provides details of our DFT and KMC analyses.

Another challenge is that most DFT analyses of thin films consider unsupported slabs due to both computational efficiency and uncertainty regarding the film-support interface; however, predictive modeling requires more demanding analysis for supported films with correct interface structure. Thus, while performing efficient exploratory analysis for unsupported slabs, we focus on judiciously selected supported thin film systems with known interface structure. In addition, we select a low-strain system as approaches for efficient precise determination of various edge diffusion barriers in the presence of significant strain are not available.

The specific systems considered here involve deposition of Au on Ag(100) thin films supported on Al-terminated NiAl(100),²⁸ and for comparison on freestanding Ag(100) slabs and bulk Ag(100). The near-perfect lattice match between fcc Au and Ag, and between Ag(100) and NiAl(100) implies minimal lateral mismatch strain. (Flat Ag(100) thin films on NiAl(100) can be created by deposition at ~ 300 K due to facile interlayer diffusion on Ag(100).⁶) Surface diffusion involves hopping of Au adatoms between nearest-neighbor (NN) 4-fold-hollow (4fh) adsorption sites through bridge-site transition states (TS). DFT analysis finds terrace diffusion barriers for isolated Au adatoms of $E_d = 0.45, 0.55$, and 0.50 eV for 1–3 ML supported Ag(100) films, $E_d = 0.55, 0.54, 0.52$, and 0.53 eV for 2–5 ML Ag(100) slabs, and $E_d = 0.53$ eV for bulk Ag(100), respectively. Diffusion barriers at island or chain edges are determined from $E_{\text{act}} = E_d + \Phi_{\text{TS}} - \Phi_{\text{init}}$, where Φ_{init} (Φ_{TS}) denotes the total lateral interaction energy in the initial state (in the TS). Φ_{init} (Φ_{TS}) is obtained by summing conventional (unconventional) ω (ϕ) interactions between the hopping adatom at its initial site (at the TS) and other adatoms at nearby 4fh sites.²⁶ See below. Our stochastic KMC simulations of Au island and chain formation include random deposition of Au and hopping between NN 4fh sites with probabilities proportional to the physical rates: $F = 0.006$ ML/s for deposition and $h = \nu e^{-E_{\text{act}}/(k_B T)}$ for hopping at surface temperature T with $\nu = 3 \times 10^{12}$ /s. We thereby track the diffusion-mediated nucleation, growth and possible coalescence of islands or chains on the surface (starting from a clean surface without any preassigned bias in the pathways for NC formation).

System thermodynamics is determined by ω interactions between adatoms at 4fh adsorption sites. For fcc(100) systems, the magnitude of second NN pair- and compact trio-interactions is usually only $\sim 10\%$ of NN pair interactions;¹⁵ however, we find stronger linear trio interactions for Au on bulk Ag(100), which are further enhanced by QSE for Ag(100) thin films, thereby guiding NC formation. The dominant ω interactions are NN attractions ($\omega_{p1} < 0$ for separation $d = a$), second NN pair interactions (ω_{p2} for $d = \sqrt{2}a$), and also linear (ω_{T1}) and bent (ω_{T2}) trio interactions. Determination of barriers for edge diffusion also requires a knowledge of ϕ interactions, with one adatom at the bridge TS for hopping and other adatoms at nearby 4fh sites. The dominant ϕ interactions are short-range pairs (ϕ_{p1} for $d = \sqrt{5}a/2$) and three types of

trios (ϕ_{T1} , ϕ_{T2} , ϕ_{T3}). See Scheme 1 and Table 1 for ω and ϕ values used in our KMC simulations.

The selected sets of interactions can be calculated directly for isolated pairs or trios of atoms in a large supercell, but this neglects some longer-range and many-body interactions. For our analysis, it is critical that the chosen ω interactions exactly recover the thermodynamic driving force for conversion of 1D chains to 2D islands. This is not achieved for any subset of directly calculated ω values. Thus, instead we use (slightly) modified effective ω values that recover exactly DFT values for the lateral interaction energy per adatom for single-atom wide chains, E_{1D} , and for a complete 2D adlayer, E_{2D} . We find that $E_{2D} < E_{1D}$ so 2D islands are always thermodynamically preferred over 1D chains for our systems. In addition, we determine the lateral interaction energy per atom for a $c(2 \times 2)$ adlayer, $E_{c(2 \times 2)}$, and for an isolated 2×2 square island, E_{square} . Then, effective ω values follow from $E_{1D} = \omega_{p1} + \omega_{T1}$; $E_{2D} = 2\omega_{p1} + 2\omega_{p2} + 2\omega_{T1} + 4\omega_{T2}$; $E_{c(2 \times 2)} = 2\omega_{p2}$; and $E_{\text{square}} = \omega_{p1} + \omega_{p2}/2 + \omega_{T2}$ (see SI).

As a preliminary analysis, we assess ω interactions for Au on bulk Ag(100) and the dependence on thickness for freestanding Ag(100) slabs. For bulk Ag(100), the linear trio attraction $\omega_{T1} = -0.065$ eV is unusually strong relative to the NN pair attraction $\omega_{p1} = -0.201$ eV ($\sim 30\%$ versus the typical $\sim 10\%$). Furthermore, ω_{T1} is enhanced due to QSE in thin Ag(100) slabs: $\omega_{T1} = -0.069, -0.088, -0.102$, and -0.087 eV compared with $\omega_{p1} = -0.164, -0.111, -0.121$, and -0.197 eV for 2–5 ML Ag(100) slabs, respectively (with ω_{T1}/ω_{p1} highest for 3–4 ML slabs). KMC simulations show that these strong ω_{T1} do guide the formation of single-atom-wide chains at 250 K, more prominently on a 4-ML slab than bulk Ag(100); see Figure 1a,b.

Behavior for supported films generally differs from that for unsupported slabs due to strain (absent for Au/Ag/NiAl(100)), differing chemical environments (a minor effect for ≥ 2 ML films), and QSE. Electron confinement in metal-on-metal films, a requirement for QSE, can still occur due to a gap or pseudo gap in the normal direction or just a depletion in the density of states near the Fermi level (as expected for NiAl); however, one expects a “phase shift” in the variation of energetics with thickness relative to that for a freestanding slab.¹⁷ Different boundary conditions for the electron wave functions at the film-substrate versus the film-vacuum interface produce this shift. We have performed computationally demanding DFT analyses of energetics for Ag(100) films on Al-terminated NiAl(100). Indeed, curves for ω versus thickness show the same trends for Ag(100) slabs and supported films but are shifted relative to each other by 1 to 2 ML. See SI Figure 1. Simulated island and

Scheme 1. Conventional (ω) and Unconventional (ϕ) Interactions between Au Adatoms Incorporated into KMC Simulations

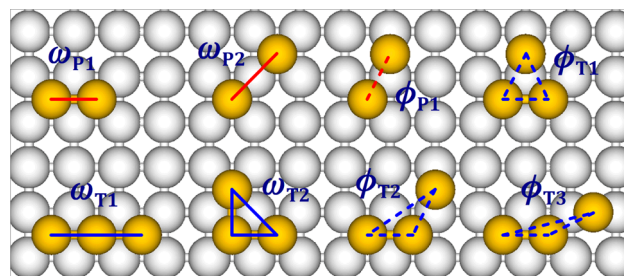


Table 1. ω and ϕ Interactions (in eV) Used in KMC Simulations for Au on 1–3 ML Supported and 4 ML Unsupported Ag(100) Films and Bulk Ag(100)

	1 ML/NiAl	2 ML/NiAl	3 ML/NiAl	4 ML	∞ ML (bulk)
ω_{p1}	−0.276	−0.131	−0.183	−0.121	−0.201
ω_{p2}	−0.006	+0.052	+0.047	+0.071	+0.030
ω_{T1}	−0.103	−0.115	−0.104	−0.102	−0.065
ω_{T2}	+0.062	+0.011	+0.011	−0.001	+0.016
ϕ_{p1}	−0.335	−0.237	−0.211	−0.130	−0.141
ϕ_{T1}	+0.244	+0.105	+0.100	+0.078	+0.044
ϕ_{T2}	+0.043	−0.013	−0.032	−0.031	−0.012
ϕ_{T3}	−0.055	−0.056	−0.073	−0.086	−0.031

chain distributions are shown in Figure 1c–e for Au deposition at 250 K on 1–3 ML supported Ag(100) films. Short chains form in all systems at 0.01–0.02 ML; however, by 0.04 ML, prominent formation of longer chains occurs only for 2-ML supported films, with a tendency to form 2D islands on 1- and 3-ML films. This behavior does not simply correlate with the strength of ω_{T1} .

One can also assess the T dependence of self-assembly. For sufficiently high T , thermodynamics should dominate producing 2D islands. For lower T , inhibited terrace diffusion should limit chain length or 2D island size. These expectations are confirmed by the KMC simulation results shown in Figure 2 for 2-ML supported films and bulk Ag(100). In both cases, 2D islands dominate at 275 K. Chain length grows upon increasing T from 225 to 250 K, especially for 2-ML supported films where 2D islands also form at 250 K.

To provide a deeper understanding of the essential features controlling chain self-assembly, we now go beyond just reporting KMC results to dissect the kinetics of key processes controlling behavior.

Chain End-to-Side Edge Diffusion. Previous studies of chain formation on anisotropic fcc(110) surfaces suggested that a key factor is anisotropic corner rounding (facile edge diffusion from chain sides-to-ends and inhibited diffusion from ends-to-sides) and inhibited detachment from chain ends (thereby blocking reattachment on sides).^{8,29,30} Earlier studies incorrectly identified anisotropic terrace diffusion as key.⁷ Thus, here we characterize edge diffusion in Figure 3a and Table 2. The barrier, E_s , for diffusion along chain sides is always much lower than E_d , and the barrier, $E_{s \rightarrow e}$, for side-to-end rounding is much

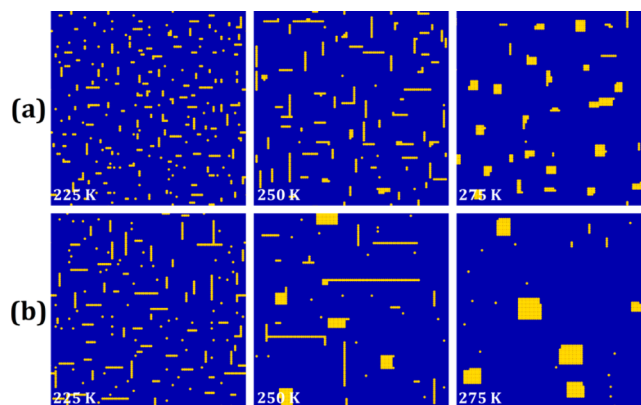


Figure 2. KMC simulations for Au island and chain formation by Au deposition at three different temperatures (225, 250, and 275 K) on (a) bulk Ag(100) and (b) 2-ML Ag(100) thin film supported by Al-terminated NiAl(100) at Au coverage of 0.05 ML. Image size: 28.9×28.9 nm².

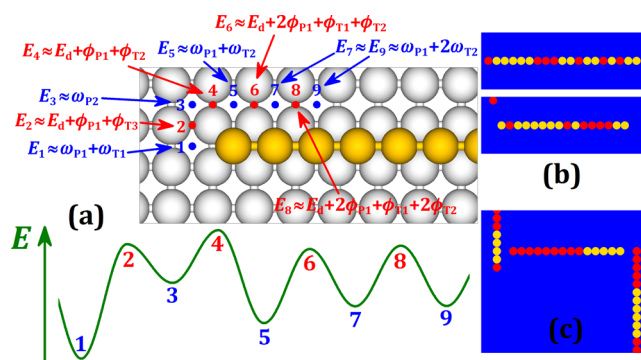


Figure 3. (a) Adsorption site and TS energies around the periphery of an Au chain. Atom-tracking KMC results for Au deposition with yellow (red) atoms deposited first (second) on: (b) 2-ML Ag(100) film supported by Al-terminated NiAl(100) and (c) bulk Ag(100).

lower than that for end-to-side rounding, $E_{e \rightarrow s}$. Thus, corner rounding is anisotropic. Of particular relevance is the rate for the slowest end-to-side rounding process, $h_{e \rightarrow s} = \nu e^{-E_{e \rightarrow s}/(k_B T)}$ relative to the typical rate $k_{agg} = F/N_{ch}$ for aggregation of deposited adatoms with individual chains for chain density N_{ch} . Naturally, k_{agg} will exceed $h_{e \rightarrow s}$ at the onset of deposition where

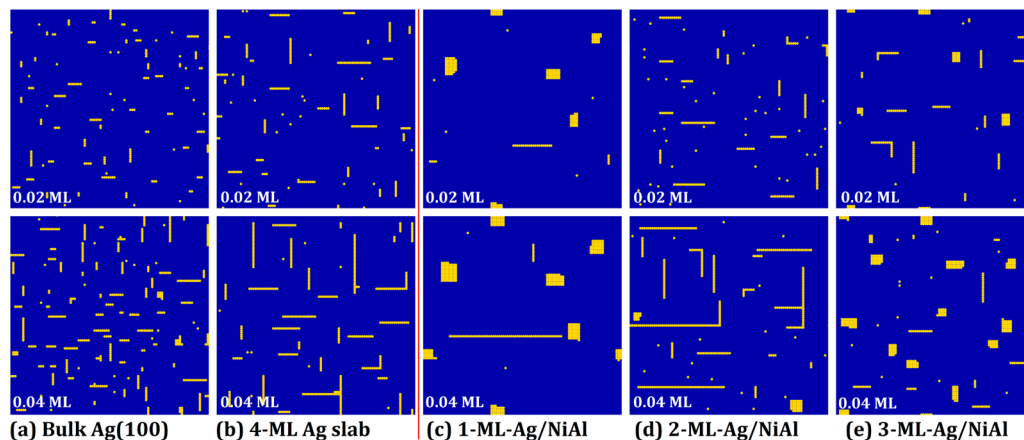


Figure 1. KMC simulations for Au island and chain formation by Au deposition at 250 K on: (a) bulk Ag(100); (b) 4-ML Ag(100) slab; and (c–e) 1–3 ML Ag(100) supported on Al-terminated NiAl(100) at Au coverages of 0.02 and 0.04 ML. Image size: 28.9×28.9 nm².

Table 2. Top Rows Report Key Barriers for Terrace (E_d), Straight Edge (E_s), End-to-Side ($E_{e \rightarrow s}$), Side-to-End ($E_{s \rightarrow e}$) Diffusion, and Detachment from Chain Ends (E_{det})^a

	1 ML/NiAl	2 ML/NiAl	3 ML/NiAl	4 ML	∞ ML (bulk)
E_d	0.449	0.553	0.501	0.515	0.530
$E_s = E_8 - E_9$	0.261	0.267	0.276	0.394	0.437
$E_{e \rightarrow s} = E_4 - E_1$	0.536	0.549	0.545	0.577	0.643
$E_{s \rightarrow e} = E_4 - E_5$	0.371	0.423	0.430	0.476	0.562
$E_{\text{det}} = E_d - E_1$	0.828	0.799	0.788	0.738	0.796
$\epsilon_2 \equiv \Delta E_{1D \rightarrow 2D}$	-0.143	-0.098	-0.149	-0.085	-0.142
ϵ_1	-0.080	+0.034	-0.090	+0.034	-0.154
$\epsilon_0 \equiv \Delta E_{2 \times 2}$	+0.222	+0.310	+0.221	+0.291	+0.099

^aLower rows relate to the energy cost $\Delta E_{n \times n} = \epsilon_0 + (n-2)\epsilon_1 + (n-2)^2\epsilon_2$ to shift $n(n-1)$ adatoms from the chain end to the side, creating an $n \times n$ square at the chain end. Note that $\epsilon_2 \equiv \Delta E_{1D \rightarrow 2D} \equiv E_{2D} - E_{1D}$ gives the preference for 2D islands over 1D chains, and $\epsilon_0 \equiv \Delta E_{2 \times 2}$ gives the energy cost for a creating a 2×2 square at the chain end. For meanings of E_1 , E_2 , ..., and E_9 , see Figure 3a.

N_{ch} is low, so edge-to-side rounding is effectively irreversible promoting initial chain formation; however, for 1–3 ML supported films (and for freestanding slabs), the rate for the slowest end-to-side rounding process, $h_{e \rightarrow s}$ at 250 K, is well above the typical $k_{\text{agg}} \approx 1.5\text{--}6/\text{s}$ for $N_{\text{ch}} \approx (1\text{--}4) \times 10^{-3}/\text{site}$ at coverage 0.04–0.1 ML with $F = 0.006$ ML/s. Thus, end-to-side rounding is facile on the time scale of chain growth. In contrast, this is not the case for Au on bulk Ag(100). Finally, the rate for detachment from chain ends, $h_{\text{det}} = \nu e^{-E_{\text{det}}/(k_B T)}$ with $E_{\text{det}} = E_d - \omega_{P1} - \omega_{T1}$ (well above $E_{e \rightarrow s}$), is always very low on the time scale of deposition, so this process is inactive.

Additional insight comes from “atom tracking” KMC.^{29,31} See Figure 3b,c. Here initially deposited Au atoms are colored yellow and subsequently deposited atoms are red. With no detachment or end-to-corner rounding, the center of chains would be yellow and the ends red; however, simulations for 2-ML supported films reveal color mixing. This reflects active end-to-side rounding: earlier deposited yellow atoms leave ends, just aggregated red atoms then join ends, and the gold atoms subsequently rejoin the end by side-to-end rounding. We find significantly less color mixing for Au deposition on bulk Ag(100) consistent with irreversible side-to-corner rounding.

To summarize, Au chain formation on bulk Ag(100) derives from effectively irreversible side-to-end rounding ($E_{e \rightarrow s} = 0.643$ eV) and negligible detachment from chain ends ($E_{\text{det}} = 0.796$ eV). For other systems, end-to-side rounding is facile (but not end detachment) except for very low coverage, and we propose that differing behavior partly derives from differing driving forces, $\Delta E_{1D \rightarrow 2D} = E_{2D} - E_{1D}$, for the formation of 2D islands from 1D chains; see Table 2. Specifically, those cases with the most prominent chain formation have the weakest driving force, but because end-to-side rounding is facile for 1-ML supported films, how can chains survive conversion to thermodynamically preferred 2D islands?

Transformation from 1D Chains to 2D Islands. Chain survival when end-to-side rounding is facile must reflect the feature that there is a significant effective barrier for the transformation of 1D chains into hybrid 1D-2D structures and finally into 2D islands. This transformation involves stochastic evolution in the complex space of possible nanocluster configurations. Thus, it is convenient to consider a simplified scenario wherein a long chain transforms to hybrid 1D–2D structures, $\{m\}$, by moving various numbers, m , of atoms from one end to one side (so m is the “reaction coordinate”). The energy cost, $\Delta E_{\{m\}}$, increases from $\Delta E_{\{0\}} = 0$ over the effective barrier before decreasing like $\Delta E_{\{m\}} \approx m\Delta E_{1D \rightarrow 2D} < 0$, for large m . Larger $|\Delta E_{1D \rightarrow 2D}|$ makes it more likely that the “biased walk” through configuration space

will evolve to a 2D island versus returning to the chain. To concretely illustrate this behavior, consider the special subset of configurations where $m = n(n-1)$ atoms at the end of a long chain are moved to form an $n \times n$ square located at the end of the chain; see Figure 4a. One can show that

$$\Delta E_{\{m\}} = \Delta E_{n \times n} = \epsilon_0 + (n-2)\epsilon_1 + (n-2)^2\epsilon_2, \text{ for } n \geq 2$$

where $\epsilon_0 \equiv \Delta E_{2 \times 2} = \omega_{P1} + 3\omega_{P2} - 2\omega_{T1} + 5\omega_{T2}$, $\epsilon_1 = 2\omega_{P1} + 4\omega_{P2} + 8\omega_{T2}$, and $\epsilon_2 \equiv \Delta E_{1D \rightarrow 2D} \equiv E_{2D} - E_{1D} = \omega_{P1} + 2\omega_{P2} + \omega_{T1} + 4\omega_{T2}$. The variation of $\Delta E_{n \times n}$ with n for supported films is shown in Figure 4b and mimics classic 2D nucleation theory.³² From Table 2, it is clear that $\Delta E_{\{m\}} = \Delta E_{n \times n}$ both increases most strongly from $\Delta E_{\{0\}} = 0$ and has the weakest large- m decrease to negative values for 2-ML-Ag/NiAl (and for 4-ML slabs) versus 1-ML- and 3-ML-Ag/NiAl. The extent of increase reflects the strength of both linear trio attractions and of second NN pair and bent trio repulsions. Thus, the transformation to 2D islands is most difficult in the first two cases.

The above analysis shows explicitly energetics of the 1D to 2D transformation pathway only for a special subset of configurations; however, there is some evidence from simulations that these configurations are relevant for the transition to 2D islands. Thus, the above behavior might reflect the minimum energy path through the complex configuration space but likely also reflects trends in energetics for more complex pathways. Note also that relative to the above quasi-equilibrium analysis, evolution from 1D chains to 2D islands is

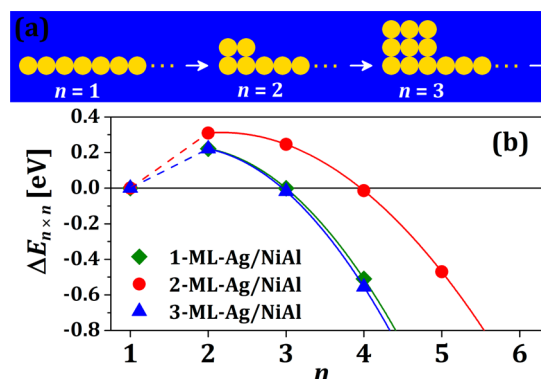


Figure 4. (a) Schematic for shifting $n(n-1)$ adatoms from a chain end to the side creating an $n \times n$ square. (b) Energy cost $\Delta E_{n \times n}$ versus n comparing Au on 1-, 2-, and 3-ML Ag(100) on Al-terminated NiAl(100).

enhanced by deposition, which creates a supersaturation of adatoms on chain sides. This feature should facilitate the formation of new rows in 2D structures.

In summary, unusually strong linear trio attractions are shown to drive the formation of single-atom wide Au chains on bulk Ag(100) and also on certain Ag(100) thin films sometimes enhanced by QSE. This behavior is demonstrated by KMC simulations of a predictive atomistic model with *ab initio* kinetics; however, deeper understanding of this behavior follows from a targeted analysis of kinetics of key edge diffusion and 1D-to-2D NC transformation processes. For Au deposited on bulk Ag(100), side-to-end rounding is effectively irreversible, naturally inducing chain formation. For Au deposited on thin Ag(100) films, modified energetics due to QSE impact chain formation. Often end-to-side rounding is facile, so chain formation and survival here is more subtle, reflecting an effective barrier for transformation from 1D to 2D structures.

■ ASSOCIATED CONTENT

■ Supporting Information

Details of our DFT calculations and KMC simulation algorithm. The Supporting Information is available free of charge on the ACS Publications website at DOI: 10.1021/acs.jpclett.5b00636.

■ AUTHOR INFORMATION

Corresponding Author

*E-mail: yhan.ameslab@gmail.com; yhan@ameslab.gov.

Notes

The authors declare no competing financial interest.

■ ACKNOWLEDGMENTS

This work was supported by NSF grants CHE-1111500 and DMR-1504593 utilizing NERSC, XSEDE, and OLCF resources. Ames Laboratory USDOE is operated by Iowa State University under Contract No. DE-AC02-07CH11358.

■ REFERENCES

- (1) Xia, Y.; Xiong, Y.; Lim, B.; Skrabalak, S. E. Shape-Controlled Synthesis of Metal Nanocrystals: Simple Chemistry Meets Complex Physics? *Angew. Chem., Int. Ed.* **2009**, *48*, 60–103.
- (2) Viswanath, B.; Kundu, P.; Halder, A.; Ravishankar, N. Mechanistic Aspects of Shape Selection and Symmetry Breaking during Nanostructure Growth by Wet Chemical Methods. *J. Phys. Chem. C* **2009**, *113*, 16866–16883.
- (3) Xia, X.; Xie, S.; Liu, M.; Peng, H.-C.; Lu, N.; Wang, J.; Kim, M. J.; Xia, Y. On the Role of Surface Diffusion in Determining the Shape or Morphology of Noble-Metal Nanocrystals. *Proc. Natl. Acad. Sci. U. S. A.* **2013**, *110*, 6669–6673.
- (4) Liao, H.-G.; Zherebetskyy, D.; Xin, H.; Czarnik, C.; Ercius, P.; Elmlund, H.; Pan, M.; Wang, L.-W.; Zheng, H. Facet Development during Platinum Nanocube Growth. *Science* **2014**, *345*, 916–919.
- (5) Michely, T.; Krug, J. *Islands, Mounds, and Atoms*; Springer: Berlin, 2004.
- (6) Evans, J. W.; Thiel, P. A.; Bartelt, M. C. Morphological Evolution during Epitaxial Thin Film Growth: Formation of 2D Islands and 3D Mounds. *Surf. Sci. Rep.* **2006**, *61*, 1–128.
- (7) Röder, H.; Hahn, E.; Brune, H.; Bucher, J.-P.; Kern, K. Building One- and Two-Dimensional Nanostructures via Diffusion Controlled Aggregation at Surfaces. *Nature* **1993**, *366*, 141–143.
- (8) Li, Y.; Bartelt, M. C.; Evans, J. W.; Waelchli, N.; Kampshoff, E.; Kern, K. Transition from One- to Two-Dimensional Island Growth on Metal (110) Surfaces Induced by Anisotropic Corner Rounding. *Phys. Rev. B* **1997**, *56*, 12539–12543.
- (9) Kalff, M.; Comsa, G.; Michely, T. How Sensitive is Epitaxial Growth to Adsorbates? *Phys. Rev. Lett.* **1998**, *81*, 1255–1258.
- (10) Wu, J.; Wang, E. G.; Varga, K.; Liu, B. G.; Pantelides, S. T.; Zhang, Z. Island Shape Selection in Pt(111) Submonolayer Homoepitaxy with or without CO as an Adsorbate. *Phys. Rev. Lett.* **2002**, *89*, 146103.
- (11) Mo, Y. W.; Kleiner, J.; Webb, M. B.; Lagally, M. G. Activation Energy for Surface Diffusion of Si on Si(001): A Scanning-Tunneling-Microscopy Study. *Phys. Rev. Lett.* **1991**, *66*, 1998–2001.
- (12) Mocking, T. F.; Bampoulis, P.; Oncel, N.; Poelsema, B.; Zandvliet, H. J. W. Electronically stabilized nanowire growth. *Nat. Commun.* **2013**, *4*, 2387.
- (13) Erwin, S. C.; Himpel, F. J. Intrinsic Magnetism at Silicon Surfaces. *Nat. Commun.* **2010**, *1*, 58.
- (14) Polei, S.; Snijders, P. C.; Erwin, S. C.; Himpel, F. J.; Meiwe-Broer, K.-H.; Barke, I. Structural Transition in Atomic Chains Driven by Transient Doping. *Phys. Rev. Lett.* **2013**, *111*, 156801.
- (15) Stasevich, T. J.; Einstein, T. L.; Stolbov, S. Extended Lattice Gas Interactions of Cu on Cu(111) and Cu(001): *Ab Initio* Evaluation and Implications. *Phys. Rev. B* **2006**, *73*, 115426.
- (16) Tiwary, Y.; Fichthorn, K. A. Connector Model for Describing Many-Body Interactions at Surfaces. *Phys. Rev. B* **2008**, *78*, 205418.
- (17) Zhang, Z.; Niu, Q.; Shih, C.-K. Electronic Growth of Metallic Overlayers on Semiconductor Substrates. *Phys. Rev. Lett.* **1998**, *80*, 5381–5384.
- (18) Han, Y.; Ünal, B.; Jing, D.; Thiel, P. A.; Evans, J. W.; Liu, D.-J. Nanoscale “Quantum” Islands on Metal Substrates: Microscopy Studies and Electronic Structure Analyses. *Materials* **2010**, *3*, 3965–3993.
- (19) Smith, A. R.; Chao, K.-J.; Niu, Q.; Shi, C.-K. Formation of Atomically Flat Silver Film on GaAs with a “Silver-Mean” Quasi Periodicity. *Science* **1996**, *273*, 226–228.
- (20) Luh, D.-A.; Miller, T.; Paggel, J. J.; Chou, M. Y.; Chiang, T.-C. Quantum Electronic Stability of Atomically Uniform Films. *Science* **2001**, *292*, 1131–1133.
- (21) Han, Y.; Ünal, B.; Qin, F.; Jing, D.; Jenks, C. J.; Liu, D.-J.; Thiel, P. A.; Evans, J. W. Kinetics of Facile Bilayer Island Formation at Low Temperature: Ag/NiAl(110). *Phys. Rev. Lett.* **2008**, *100*, 116105.
- (22) Ma, L.-Y.; Tang, L.; Guan, Z.-L.; He, K.; An, K.; Ma, X.-C.; Jia, J.-F.; Xue, Q.-K.; Han, Y.; Huang, S.; Liu, F. Quantum Size Effect on Adatom Surface Diffusion. *Phys. Rev. Lett.* **2006**, *97*, 266102.
- (23) Song, C.-L.; Wang, Y.-L.; Ning, Y.-X.; Jia, J.-F.; Chen, X.; Sun, B.; Zhang, P.; Xue, Q.-K.; Ma, X. Tailoring Phthalocyanine Metalation Reaction by Quantum Size Effect. *J. Am. Chem. Soc.* **2010**, *132*, 1456–1457.
- (24) Aballe, L.; Barinov, A.; Locatelli, A.; Heun, S.; Kiskinova, M. Tuning Surface Reactivity via Electron Quantum Confinement. *Phys. Rev. Lett.* **2004**, *93*, 196103.
- (25) Ma, X.; Jiang, P.; Qi, Y.; Jia, J.; Yang, Y.; Duan, W.; Li, W.-X.; Bao, X.; Zhang, S. B.; Xue, Q.-K. Experimental Observation of Quantum Oscillation of Surface Chemical Reactivities. *Proc. Natl. Acad. Sci. U. S. A.* **2007**, *104*, 9204–9208.
- (26) Han, Y.; Ünal, B.; Evans, J. W. Formation of a Novel Ordered Ni₃Al Surface Structure by Codeposition on NiAl(110). *Phys. Rev. Lett.* **2012**, *108*, 216102.
- (27) Han, Y.; Liu, D.-J.; Evans, J. W. Real-Time *Ab Initio* KMC Simulation of the Self-Assembly and Sintering of Bimetallic Epitaxial Nanoclusters: Au + Ag on Ag(100). *Nano Lett.* **2014**, *14*, 4646–4652.
- (28) Lerch, D.; Dössel, K.; Hammer, L.; Müller, S. Point Defects in the NiAl(100) Surface. *J. Phys.: Condens. Matter* **2009**, *21*, 134007.
- (29) Ferrando, R.; Hontinfinde, F.; Levi, A. C. Morphologies in Anisotropic Cluster Growth: A Monte Carlo Study on Ag(110). *Phys. Rev. B* **1997**, *56*, R4406–R4409.
- (30) Mottet, C.; Ferrando, R.; Hontinfinde, F.; Levi, A. C. A Monte Carlo Simulation of Submonolayer Homoepitaxial Growth on Ag(110) and Cu(110). *Surf. Sci.* **1998**, *417*, 220–237.
- (31) Han, Y.; Russell, S. M.; Layson, A. R.; Walen, H.; Yuen, C. D.; Thiel, P. A.; Evans, J. W. Anisotropic Coarsening: One-Dimensional Decay of Ag Islands on Ag(110). *Phys. Rev. B* **2013**, *87*, 155420.

(32) Gunton, J. D.; Droz, M. *Introduction to the Theory of Metastable and Unstable States, Lecture Notes in Physics*; Springer: Berlin, Vol. 183, 1983.

Supporting Information

for “Directing Anisotropic Assembly of Metallic Nanoclusters by Exploiting Linear Trio Interactions and Quantum Size Effects: Au Chains on Ag(100) Thin Films”

Yong Han and James W. Evans

Department of Physics and Astronomy, and Division of Chemical and Biological Sciences, Ames Laboratory—U. S. Department of Energy, Iowa State University, Ames, Iowa 50011, USA

Density functional theory (DFT) Analysis

Our DFT total energy calculations were performed by using the plane-wave VASP code [1-4] with slab geometries representing the surface. Here, slabs with a specific lateral supercell size (described below) and various arrangements of adsorbates on one side (the “top” side) are repeated periodically in the plane of the slab. In the orthogonal direction, slabs separated by a vacuum region and also repeated periodically. The vacuum thickness between adjacent slabs is always greater than 1.5 nm, which was shown to be thick enough for energy convergence (i.e., to eliminate significant interaction between adjacent slabs). We use the projector augmented wave (PAW) method [5, 6] for the electron-core interactions, and the PBE-GGA [7] for exchange and correlation. The corresponding pseudopotentials (PPs) were generated by the VASP group, and described as the “standard” PPs to differentiate them from newly-released PPs in 2013. The energy cutoffs for the plane wave basis are set to be default values of VASP code (249.846 eV for Au-Ag system, and 269.533 eV for Au-Ag-Ni-Al system). During the optimization/relaxation of atomic positions, the bottommost layer of the slab is always fixed and other atoms are allowed to relax until the self-consistent forces reach the tolerance of 0.1 eV/nm. (Thus, the fixed layer is an Ag layer for the freestanding Ag(100) films, and an Al layer for a 5-ML Al-terminated NiAl(100) slab which is used to support an Ag(100) thin film.) For the fixed layer, and also for the other layers in the slab before relaxation, we use the theoretical lattice constant, $a_{\text{Ag}} = 0.4166$ nm for Ag(100), and $a_{\text{NiAl}} = 0.2896$ nm for NiAl(100). Finally, to assess energetics for Au on bulk Ag(100), DFT results for Ag(100) slabs were averaged over a range of large thicknesses (7-12 ML) which appears to be an effective way to eliminate QSE and to extrapolate to bulk behavior. Selection of supercell size and the corresponding Γ -centered \mathbf{k} mesh depends on the quantities being analyzed, as described below.

First, we comment on our direct calculation of conventional (ω -) and distinct unconventional (ϕ -) interactions for isolated pairs and triples of adatoms. Here, first pair interactions are determined for all relevant separations. Values for these are obtained from the total system energy, E_{tot} , with a pair of adatoms by subtracting the slab energy and twice the adsorption energy for isolated adatoms, E_{ads} . Then, trio interactions are obtained from E_{tot} with a triple of adatoms by subtracting the slab energy, three times E_{ads} , and also all pair interactions occurring within the triple of adatoms. For this analysis, we use a large lateral supercell size (10×10). The \mathbf{k} mesh is taken to be $5 \times 5 \times 1$. Such calculations are expensive because of the large supercell, in particular for systems with an Ag(100) film supported on a NiAl(100) substrate. After a series of convergence tests with varying

thicknesses of Al-terminated NiAl(100) slabs, we selected a 5-ML slab as the substrate in the Au/Ag(100)/NiAl(100) system. Note that we use an Al-terminated rather than a Ni-terminated NiAl(100) slab since a preference for the Al-termination is broadly recognized [8]. However, actual surface depends on sample preparation and on any slight deviation from stoichiometry in the bulk crystal, and surface defects can occur, e.g., anti-site Ni. Our results show that the strength of the dominant interactions illustrated in Scheme 1 (of a few 10's to 100's of meV) is significantly greater than the strength of the longer-range pair and less compact trio interactions (from a few meV to of the order of ten meV) which can be attractive or repulsive.

As described in the text, we do not use any finite set of these directly calculated DFT values for ω -interactions as the input in our KMC simulations, as such a finite (truncated) set will not exactly recover the key thermodynamic driving force to convert long chains to large 2D adatom islands. Instead, to exactly incorporate this driving force, we use four effective values for ω_{P1} , ω_{P2} , ω_{T1} , and ω_{T2} (see Scheme 1 for these interactions) which are selected to recover exactly the following interaction energies per Au adatom: E_{1D} for a 1D chain, E_{2D} for a 2D 1 \times 1 adlayer, $E_{c(2\times 2)}$ for a c(2 \times 2) adlayer, and E_{square} for an isolated 2 \times 2 adatom square, by solving the equations listed in the text. As an aside, we have checked sensitivity of the resulting values of the four effective ω -interactions to choice of four configurations whose energies are used to determine them. For example, if we retain the 1D chain, 2D 1 \times 1 adlayer, and c(2 \times 2) adlayer, but replace the isolated square by a double chain, we find little change in these values. For the 1D chain, we use a lateral 10 \times 1 supercell with a \mathbf{k} mesh of 5 \times 35 \times 1. For the 2D 1 \times 1 and c(2 \times 2) adlayer structures, \mathbf{k} meshes are taken to be 35 \times 35 \times 1, and 21 \times 21 \times 1, respectively. For an isolated 2 \times 2 square island, the lateral supercell size is 10 \times 10 with the \mathbf{k} mesh of 5 \times 5 \times 1. The above strategy constitutes a standard “cluster expansion” type approach for determining metal adatom interactions [9]. However, we select configurations for DFT analysis to ensure that the effective interactions recover exactly the above-mentioned key system thermodynamics.

Next, we compare results for ω -interactions obtained from direct calculation versus effective values from the cluster expansion approach. Table S1 lists the ω -interaction ratios for Au on 2 - 5 ML Ag(100) films, and Au on 1 - 3 ML Ag(100) films supported on Al-terminated NiAl(100). The superscript “DFT” denotes the ω -interaction value from direct calculations using a large lateral supercell size of 10 \times 10, and the superscript “EFF” denotes the effective ω -interaction values. From Table S1, the ratios $\omega_{P1}^{\text{EFF}}/\omega_{P1}^{\text{DFT}}$ and $\omega_{T1}^{\text{EFF}}/\omega_{T1}^{\text{DFT}}$ are around 1, indicating the effective values are comparable to those directly from the large-supercell calculations. We should note that the magnitude of values for ω_{P2} and ω_{T1} are significantly smaller than for ω_{P1} and ω_{T2} . Thus, the magnitude of the absolute uncertainty in the DFT prediction of the former is larger, and there is generally a greater deviation between EFF and DFT values.

Now, we briefly comment further on determination of unconventional ϕ -interactions which reflect interaction of a hopping adatom at the bridge site transition state with other nearby adatoms at four-fold-hollow adsorption sites. Focusing on chain or island formation, it should suffice to include just the four dominant ϕ -interactions, ϕ_{P1} , ϕ_{T1} , ϕ_{T2} , and ϕ_{T3} , (shown in Scheme 1 in the text) and neglect other ϕ -interactions. When calculating ϕ -interactions, we specifically fix the x - or y - coordinate (parallel to surface aligned with the

two surface atoms forming the bridge site) of the Au adatom on the bridge site to avoid motion of the adatom towards its neighboring 4-fold-hollow site. This would generally occur due to the asymmetry induced by the local adatom environment.

Table S1. The ω -interaction ratios for Au on unsupported 2 - 5 ML Ag(100) films, and for Au on 1 - 3 ML Ag(100) films supported on Al-terminated NiAl(100).

Ag(100)	$\omega_{P1}^{EFF}/\omega_{P1}^{DFT}$	$\omega_{T1}^{EFF}/\omega_{T1}^{DFT}$
2 ML	0.857	1.316
3 ML	1.002	0.808
4 ML	0.872	0.869
5 ML	0.899	1.189
1 ML/NiAl	0.913	1.123
2 ML/NiAl	0.930	0.814
3 ML/NiAl	0.987	1.012

It is appropriate to also note that from analysis using the PBEsol functional [10], we find that interaction energy magnitudes are on average increased by about 20% relative to those determined with the PBE functional. Our previous analysis for the Ag/Ag(100) system suggests that the higher PBEsol values more accurately reflect adlayer interactions in fcc metal systems. Thus, in the KMC simulations reported in the text, the input interactions listed in Table I and Table S1 are obtained by taking the values obtained from extensive PBE analysis and multiplying by a factor of 1.23. The differences between PBE and PBEsol values of interactions, and also the differences between directly calculated versus effective values, prompt the question of whether self-assembly behavior depends strongly on the choice of energetic input to the KMC simulations of Au deposition. In fact, we have performed simulations with three distinct choices of interactions (effective PBEsol, effective PBE, and directly calculated PBEsol). In all choices, we find common trend: chain formation at 250 K and below for lower Au coverages; and 2D island formation at higher temperatures and higher coverages. Some details of these features and their relative prominence for different systems depend on the choice of interactions.

We also performed selected analyses with the newly-updated PAW-PBE PPs (released in 2013) from the VASP group. We obtained a slightly different lattice constant of 0.4152 nm for Ag (cf., the above $a_{Ag} = 0.4166$ nm), while for NiAl it is 0.2895 nm (almost the same as above $a_{NiAl} = 0.2896$ nm). Using the updated version of PPs, we also analyzed the adsorption energy difference between bridge and hollow sites to determine E_d for Au on Ag(100), and found no significant changes from results with the “standard” PPs. Using PBEsol with updated potentials, we obtain a lattice constant of 0.4054 nm for Ag, and

0.2864 nm for NiAl (cf., experimental values: 0.4069 nm for Ag at 0 K [11, 12], and 0.2887 nm for NiAl at room temperature [13, 14]).

Our modeling did not include exchange of Au with an Ag atom in the top layer of Ag(100) as the associated barrier, E_{ex} , is prohibitively high. For example, for a 1-ML Ag(100) film supported on NiAl(100), we performed analyses using 3×3 and 4×4 supercell sizes using the climbing NEB approach [15, 16] to obtain estimates of the exchange barriers of 0.756 and 0.724 eV, respectively. The slightly lower latter value presumably reflects more facile relaxation of the region surrounding the exchange event for the larger supercell. The \mathbf{k} mesh is $15 \times 15 \times 1$ for both cases. Setting $\delta E = E_{\text{ex}} - E_{\text{d}} \approx 0.28$ eV, this implies a diffusion length $L_{\text{ex}} = ae^{-\delta E/(k_{\text{B}}T)}$ of Au before exchange, where $a \approx 0.289$ nm is the surface lattice constant. This L_{ex} is sufficiently large that Au adatoms aggregate into nanoclusters before exchanging.

Discussion of Quantum Size Effects (QSE) in Ag(100) thin film systems

QSE is relevant for metal-on-metal films as well as metal-on-semiconductor films, since electron confinement is still possible in the former case. As discussed in the text, this confinement can result from various features, e.g., a gap or pseudo gap in the direction normal to the interface, or just a depletion in the density of states of the support near the Fermi level (as expected for NiAl). However, in general one expects a “phase-shift” in the variation of energetics with thickness relative to an unsupported slab. In a simple free electron gas treatment for the film, one solves Schrödinger equation with different boundary conditions at the film-substrate interface for the supported film versus the film-vacuum interface for the slab. This can result in a shift in distinctive features of behavior (e.g., a local minimum in surface energy) to different thickness.

For epitaxial growth by deposition on supported thin films, various effects can contribute to a dependence of the thickness of the supported film. Deconvolution of these effects is in general non-trivial. Specifically, QSE, strain, and chemical bonding variation can all contribute to such a thickness dependence. Strain effects are eliminated in our system due to an excellent lattice match of fcc Au and Ag, and also of Ag(100) and NiAl(100). However, with regard to chemical bonding variation, top layer Ag in supported films is bound below to Al for 1 ML films, but to Ag for ≥ 2 ML films. These different chemical environments which could influence Au adatom interaction energetics. Nonetheless, strong evidence that QSE indeed controls the thickness variation for ≥ 2 ML supported films (where top layer Ag is always bound below to Ag) follows from the similar variation with thickness in Au interaction energies to that observed for unsupported Ag(100) slabs.

More specifically, as shown in Figure S1, while one sees the same trends in variation of the various ω 's with thickness, there is a “phase shift” between behavior for unsupported and supported slabs, where the same feature appear for a 1-2 ML greater film thickness for the unsupported relative to the supported films. Analogous behavior is seen in other similar systems, e.g., comparing Ag(100) slabs and supported Ag/Fe(100) films [17].

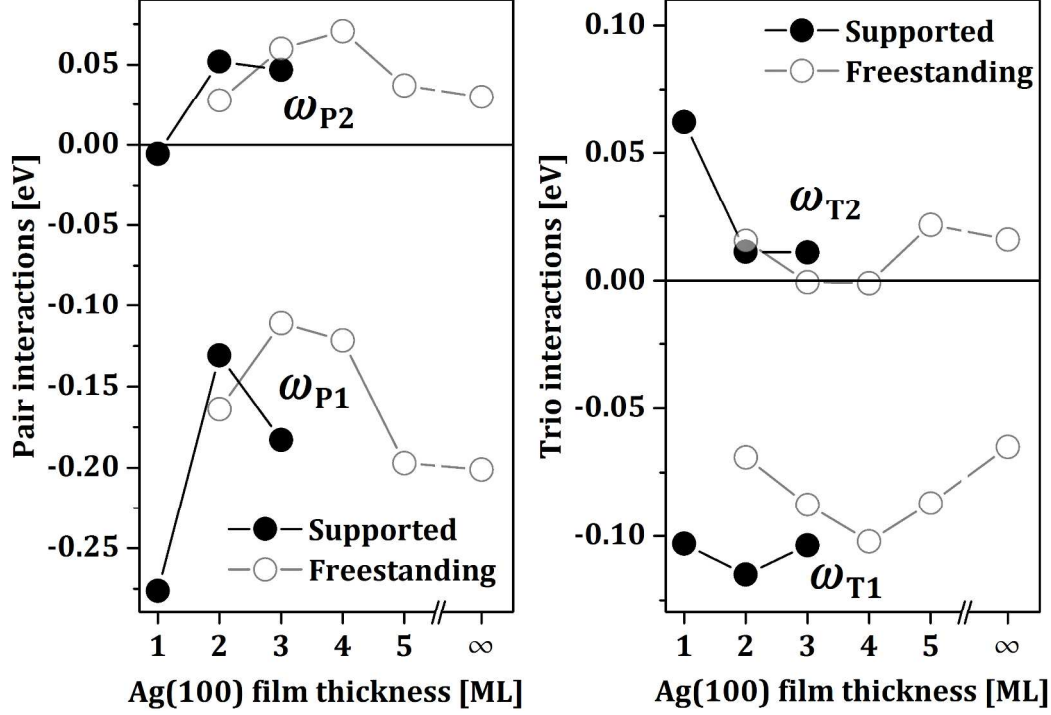


Figure S1. Comparison of the variation with thickness of conventional Au interactions for unsupported Ag(100) slabs and supported Ag(100) films on Al-terminated NiAl(100). Note that the same general trends appear, but with a “phase shift” to 1-2 ML greater film thickness for the unsupported slab.

Kinetic Monte Carlo (KMC) simulation algorithm

We briefly describe our KMC simulation algorithm which is consistent with the prescribed stochastic lattice-gas model for the deposition and diffusion-mediated self-assembly of Au nanoclusters on Ag(100) thin films. The basic requirement of the algorithm is simply to implement various processes (deposition, hopping of adatoms between neighboring four-fold-hollow sites in various local environments) with probabilities proportional to their physical rates. The rate of deposition per site is a constant, F . The numerous rates for adatom hopping are given by the generic formula $h = \nu e^{-E_{\text{act}}/(k_B T)}$ with $E_{\text{act}} = E_d + \Phi_{\text{TS}} - \Phi_{\text{init}}$. Here Φ_{init} (Φ_{TS}) is determined from summing appropriate ω - (ϕ -) interactions, as described in the text. The simulation approach implemented is a Bortz-Kalos-Lebowitz (BKL)-type rejection-free algorithm [18].

Our BKL-type algorithm for deposition and diffusion-mediated assembly is implemented for a system with $L \times L$ surface adsorption sites, which are labeled (i, j) , and periodic boundary conditions. We determine the total deposition rate $R_{\text{dep}} = FL^2$, and track the total hopping rate $R_{\text{hop}} = \sum_{k=1}^{N_{\text{hop}}} R_k$, where N_{hop} is the number of adatoms which can potentially hop (if they are not surrounded by four occupied sites), and R_k is the total hop rate for the k^{th} such adatom. Thus, the total rate for all processes in the system is $R_{\text{tot}} = R_{\text{dep}} + R_{\text{hop}}$, and this changes during the simulation since R_{hop} changes. A random number, ξ , is selected uniformly distributed on $[0, 1]$. If $\xi < R_{\text{dep}}/R_{\text{tot}}$, one implements

deposition, and otherwise hopping. For the former, one randomly selects one of the L^2 adsorption sites, (i, j) , with the aid of two random numbers (one to select i and the other j). If hopping is selected, another random number, ξ , is selected. If $R_1 + R_2 + \dots + R_{k-1} < \xi R_{\text{hop}} \leq R_1 + R_2 + \dots + R_k$, one selects the k^{th} adatom for hopping. Then, one must select one of up to four possible directions ($\alpha = 1, 2, 3$, or 4) to move this adatom. If the corresponding hop rates are $R_k(\alpha)$, a random number ξ is selected, and the direction of hopping is chosen as $\alpha = 1$ if $\xi R_k \leq R_k(1)$, as $\alpha = 2$ if $R_k(1) < \xi R_k \leq R_k(2)$, etc. In our simulation, it is not particularly important to track physical time as typically we run the simulation until a specified amount of Au is deposited. However, time, t , is readily tracked, being incremented by an amount $\Delta t = -\ln(\eta)/R_{\text{tot}}$ for each deposition or hopping event, where η is a random number uniformly distributed on $[0,1]$.

REFERENCES

- [1] Kresse, G.; Hafner, J. *Phys. Rev. B* **1993**, *47*, 558.
- [2] Kresse, G.; Hafner, J. *Phys. Rev. B* **1994**, *49*, 14251.
- [3] Kresse, G.; Furthmüller, J. *Comput. Mat. Sci.* **1996**, *6*, 15.
- [4] Kresse, G.; Furthmüller, J. *Phys. Rev. B* **1996**, *54*, 11169.
- [5] Blochl, P. E. *Phys. Rev. B* **1994**, *50*, 17953.
- [6] Kresse, G.; Joubert, D. *Phys. Rev. B* **1999**, *59*, 1758.
- [7] Perdew, J. P.; Burke, K.; Ernzerhof, M. *Phys. Rev. Lett.* **1996**, *77*, 3865.
- [8] Lerch, D.; Dössel, K.; Hammer, L.; Müller, S. *J. Phys.: Condens. Matter* **2009**, *21*, 134007.
- [9] Stasevich, T. J.; Einstein, T.L; Stolbov, S. *Phys. Rev. B* **2006**, *73*, 115426.
- [10] Perdew, J. P.; Ruzsinszky, A.; Csonka, G. I.; Vydrov, O. A.; Scuseria, G. E.; Constantin, L. A.; Zhou, X.; Burke, K. *Phys. Rev. Lett.* **2008**, *100*, 136406.
- [11] Giri A. K.; and Mitra, G. B. *J. Phys. D: Appl. Phys.* **1985**, *18*, L75.
- [12] Shoenberg, D. *Phil. Trans. R. Soc. Lond. A* **1962**, *255*, 85.
- [13] Noebe, R. D.; Bowman, R. R.; Nathal, M. V. *Int. Mater. Rev.* **1993**, *38*, 193.
- [14] Taylor, A.; Doyle, N. J. *J. Appl. Cryst.* **1972**, *5*, 201.
- [15] Henkelman, G.; Uberuaga, B. P.; Jónsson, H. *J. Chem. Phys.* **2000**, *113*, 9901.
- [16] Henkelman, G.; Jónsson, H. *J. Chem. Phys.* **2000**, *113*, 9978.
- [17] Wei, C. M.; Chou, M. Y. *Phys. Rev. B* **2003**, *68*, 125406.
- [18] Bortz, A. H.; Kalos, M. H.; Lebowitz, J. L. *J. Comp. Phys.* **1975**, *17*, 10.